Nonlinear Wavefield Characteristics of Seismic Translation and Rotation in Small-Strain Deformation from Moment Tensor Simulations

Wei Li [1,2], Yun Wang [1,2,*], Chang Chen[1,2], Lixia Sun[1,3]

[1] *"MWMC" group, School of Geophysics and Information Technology, China University of Geosciences, Beijing 100083, China*

[2] *State Key Laboratory of Geological Processes and Mineral Resources, China University of Geosciences, Beijing 100083, China*

[3] *Sinopec Research Institute of Petroleum Engineering Co., Ltd., Beijing 102206, China*

[*] Corresponding author: wangyun@mail.gyig.ac.cn.

Abstract Seismic rotational motions recorded in near-field and strong-motion observations show discrepancies with theoretical predictions derived from linear elastodynamic theory. To investigate potential nonlinear contributions, this study incorporates geometric nonlinear effects into wave propagation theory using the Green-Lagrange strain tensor. A staggered-grid finite-difference method is used to simulate six-component (translational and rotational) wavefields generated by three basic moment-tensor source types: isotropic (ISO), double-couple (DC), and compensated linear vector dipole (CLVD). The results demonstrate that nonlinear effects, as a secondary source, have a universal intensity pattern adhering to the physics of wave motion. However, the efficiency of exciting these effects and the

23   modulation of wavefield attributes (such as P-wave polarization) depend strongly on

24   source type. Simulations show that rotational components exhibit higher sensitivity to

25   nonlinear effects driven by S-waves. Reference simulations of two moderate-to-strong

26   earthquakes suggest that surface waves are the primary carriers of nonlinear features.

28   1 Introduction

29   Seismic rotational motion is a significant part of ground shaking, particularly

30   recordable in strong-motion events (Graizer, 1991; 2010; Zhou et al., 2019). Under

31   near-field and shallow-source conditions, these rotational motions exhibit pronounced

32   characteristics (Kozak, 2009; Sun et al., 2017) and play a critical role in the seismic

33   design and stability assessment of structures (Li, 1991; Yan, 2017; Huras et al., 2021).

34   Progress in research indicates that incorporating rotational motion data, which

35   contains information on the spatial gradients of the wavefield, can improve the

36   accuracy and stability of seismic source inversion (Bernauer et al., 2014; Donner,

37   2016; Ichinose et al., 2021; Hua and Zhang, 2022).

38   In a review of advances in rotational seismology, Lee et al. (2009) suggested

39   that the measured rotational components in strong ground motion may originate from

40   nonlinear elasticity and site effects. This suggestion is based on empirical evidence

41   from observations in Japan and Taiwan, where rotational measurements are typically

42   one to two orders of magnitude larger than those expected from classical linear

43   elasticity theory or derived from translational data, indicating the limitations of linear

44   theory. In geophysics, nonlinearity often refers to constitutive nonlinearity related to

45   material behavior, such as the hysteretic and elastoplastic responses of soils and rocks

46   under large strains (Frankel et al., 2002; Bonilla et al., 2005; 2011; Régnier et al.,

47   2018). This type of nonlinearity involves intrinsic energy dissipation and plastic

48   deformation, resulting in nonlinear site amplification in strong-motion records

49   (Régnier et al., 2018).

50 On the other hand, nonlinearity can also arise from the geometric description of

51 an object's deformation itself, known as geometric nonlinearity. Even if a material

52 adheres to Hooke's law, the mathematical relationship between strain and

53 displacement can still contain higher-order nonlinear terms. This geometric

54 nonlinearity is significant when describing seismic wave propagation in pre-stressed

55 media (Tromp and Trampert, 2018). However, current research has predominantly

56 focused on material constitutive nonlinearity and its linearized approximation

57 (Renaud et al., 2012; 2013; TenCate et al., 2016; Feng et al., 2018), with a systematic

58 investigation into the strain nonlinearity introduced by the measure of deformation,

59 and its expression in seismic wave propagation, is still lacking. This neglected aspect

60 may contribute to understanding the complex rotational motions observed in the near

61 field of strong earthquakes.

62 Therefore, this study aims to systematically characterize geometric nonlinear

63 effects within the framework of the small-strain assumption by incorporating the

64 Green-Lagrange strain tensor. We employ a staggered-grid finite-difference method to

65 simulate three fundamental moment tensor sources, exploring how geometric

66 nonlinearity leads to body-wave coupling and energy redistribution, and its intrinsic

67 dependence on the source type. Furthermore, using two moderate-to-strong

68 earthquakes in the Taiwan region as examples, we explore the manifestation of

69 nonlinear effects in a more complex scenario.

70 2 Theory and method

71 2.1 Elastodynamic theory

72 Consider a three-dimensional (3D) elastic medium in an orthogonal Cartesian

73 coordinate system (Fig. 1). An infinitesimal line element connecting a particle A at

74 position **x** and an adjacent particle B at **x**+d**x** has an initial length of ds. When

75 subjected to external force, this element undergoes a displacement $\boldsymbol{u}(\boldsymbol{x}, t)$, moving to

76 new positions A' and B' at **x'** and **x'**+d**x'**, respectively, with a deformed length of ds'.

77 This process includes both rigid-body displacement and strain-induced distortion. The

78 strain energy density can be characterized by the quadratic form of the change in the

79 element's length, as shown in Eq. (1).

80
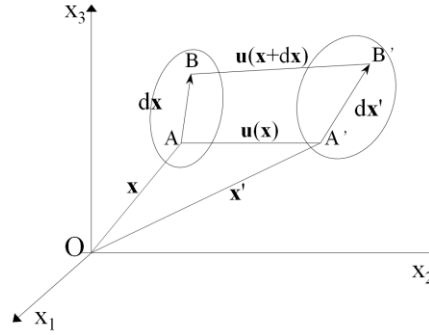
81 **Figure 1.** Schematic diagram of displacement and deformation of an infinitesimal line

82 element in an elastic medium (adapted from Aki and Richards (2002))

$$(ds')^2 - (ds)^2 = 2E_{ij}dx_i dx_j, \ i, j \in \{1, 2, 3\} \tag{1}$$

84 where E_{ij} is the Green-Lagrange strain tensor, which provides an objective measure of

85 deformation. In Cartesian coordinates, E_{ij} is defined by the displacement field as:

$$E_{ij} = \frac{1}{2}(\frac{\partial u_j}{\partial x_i} + \frac{\partial u_i}{\partial x_j} + \frac{\partial u_k}{\partial x_i} \cdot \frac{\partial u_k}{\partial x_j}), \ i, j, k \in \{1, 2, 3\} \tag{2}$$

87 The displacement gradient tensor can be decomposed into a symmetric strain

88 tensor (e_{ij}) and an antisymmetric rotation tensor (r_{ij}):

89
$$\frac{\partial u_j}{\partial x_i} = e_{ij} + r_{ij} \tag{3}$$

90 where,

91
$$e_{ij} = \frac{1}{2}(\frac{\partial u_j}{\partial x_i} + \frac{\partial u_i}{\partial x_j}), \quad r_{ij} = \frac{1}{2}(\frac{\partial u_i}{\partial x_j} - \frac{\partial u_j}{\partial x_i}) \tag{4}$$

92 Traditional linear elasticity simplifies the problem by neglecting the second-order

93 product of displacement gradients in Eq. (2), thus reducing the Green-Lagrange strain

94 tensor to the strain tensor e_{ij}:

95
$$E_{ij} \approx e_{ij} = \frac{1}{2}(\frac{\partial u_j}{\partial x_i} + \frac{\partial u_i}{\partial x_j}) \tag{5}$$

96 For an isotropic medium, the stress-strain constitutive relationship is linear

97 (generalized Hooke's law), given by Eq. (6), where λ and μ are the Lamé constants.

98
$$\sigma_{ij} = \lambda\delta_{ij}e_{kk} + 2\mu e_{ij} \tag{6}$$

99 The theoretical framework of this study consistently employs the linear

100 constitutive relationship described by Eq. (6). However, the complete Green-Lagrange

101 strain tensor E_{ij} (rather than its linear approximation e_{ij}) is substituted into it, yielding

102 a stress expression that reflects geometric nonlinearity:

103
$$\sigma_{ij} = \lambda\delta_{ij}e_{kk} + 2\mu e_{ij} + \underbrace{\frac{1}{2}\lambda\delta_{ij}(\frac{\partial u_k}{\partial x_m} \cdot \frac{\partial u_k}{\partial x_m}) + \mu\frac{\partial u_k}{\partial x_i} \cdot \frac{\partial u_k}{\partial x_j}}_{\text{additional terms}}, \quad i, j, k, m \in \{1, 2, 3\} \tag{7}$$

104 Substituting this stress expression into the momentum conservation law (Eq. (8)),

105
$$\rho\frac{\partial^2 u_i}{\partial t^2} = \frac{\partial \sigma_{ij}}{\partial x_j} \tag{8}$$

106 where ρ is the medium density, we finally obtain the nonlinear wave equation:

107
$$\rho\frac{\partial^2 u_i}{\partial t^2} = \underbrace{\left(\lambda+\mu\right)\frac{\partial^2 u_j}{\partial x_i \partial x_j} + \mu\frac{\partial^2 u_i}{\partial x_j \partial x_j}}_{\text{original terms}} + \underbrace{\lambda\frac{\partial u_k}{\partial x_i}\frac{\partial^2 u_k}{\partial x_j x_j} + \mu\left(\frac{\partial^2 u_k}{\partial x_i x_j}\frac{\partial u_k}{\partial x_j} + \frac{\partial^2 u_k}{\partial x_j x_j}\frac{\partial u_k}{\partial x_i}\right)}_{\text{additional terms}}, \; i,j,k \in \{1,2,3\} \quad (9)$$

108   In Eq. (9), under the small-strain assumption, the original terms constitute the

109   classic wave equation, while the subsequent additional terms arise from the geometric

110   nonlinearity of strain. These additional terms mathematically act as endogenous,

111   secondary body force sources that depend on the wavefield itself. In linear theory,

112   P-waves (driven by the divergence field, representing volume change) and S-waves

113   (driven by the curl field, representing shape change) are strictly decoupled. However,

114   the existence of these nonlinear terms disrupts this decoupling. Specifically, the term

115    $\partial u_k/\partial x_i \cdot \partial u_k/\partial x_j$ is a product of displacement gradients (which include both strain and

116   rotation). When the P-wave (dominated by compressional strain) propagates, its

117   non-uniform strain field generates spatial gradients. Through these higher-order terms,

118   the gradient field of the P-wave can generate an equivalent body force source with a

119   curl component within the medium, which in turn radiates S-waves. The reverse is

120   also true. This is the fundamental physical mechanism of P-S mode conversion:

121   energy is transferred between the compressional and shear modes through the

122   self-interaction of the wavefield.

123   2.2 Staggered-grid finite-difference method

124   To solve the nonlinear wave equation (9), we employ a high-accuracy

125   Staggered-Grid Finite-Difference (SGFD) method (Virieux, 1986; Sun et al., 2018).

126   First, by taking the time derivative of the nonlinear constitutive relation (7) and

127   combining it with the momentum conservation equation (8), we convert the

128   second-order wave equation into a system of first-order velocity-stress partial

129   differential equations. This system includes additional stress-rate terms generated by

130   the second-order products of displacement gradients. These terms update the

131   displacement field through time integration of the velocity field, thereby

132   implementing the nonlinear coupling. The resulting velocity-stress equations are:

133
$$\begin{cases} \rho \dfrac{\partial v_i}{\partial t} = \dfrac{\partial \sigma_{ij}}{\partial x_j} \\[2mm] \dfrac{\partial \sigma_{ij}}{\partial t} = \lambda \delta_{ij} \dfrac{\partial E_{kk}}{\partial t} + 2\mu \dfrac{\partial E_{ij}}{\partial t} \\[2mm] \quad = \lambda \delta_{ij} \dfrac{\partial v_k}{\partial x_k} + \mu(\dfrac{\partial v_i}{\partial x_j} + \dfrac{\partial v_j}{\partial x_i}) + \underbrace{\lambda \delta_{ij}(\dfrac{\partial v_k}{\partial x_m} \cdot \dfrac{\partial u_k}{\partial x_m}) + 2\mu \dfrac{\partial v_k}{\partial x_i} \cdot \dfrac{\partial u_k}{\partial x_j}}_{\text{additional terms}} \end{cases} \quad , i,j,k,m \in \{\mathrm{x,y,z}\} \qquad (10)$$

134   where $v_i = \partial u_i / \partial t$. In the SGFD scheme, different physical quantities are staggered

135   on the spatial grid cells. This arrangement naturally satisfies the central-difference

136   approximation for differential operators, effectively suppressing numerical dispersion

137   and enhancing computational stability and accuracy, as illustrated in Fig. 2.

138
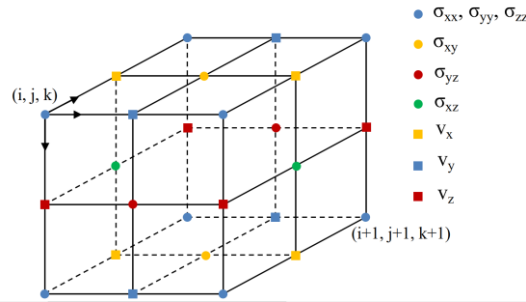
139   **Figure 2.** 3D staggered-grid configuration for velocity-stress formulations,

140   showing the placement of velocity components and stress components.

141   To handle the model's truncated boundaries, we employ the Perfectly Matched

142   Layer (PML) absorbing boundary condition (Li et al., 2015). For simulations

143   involving a free surface, the free boundary is implemented at the top of the model by

144 setting the acoustic boundary replacement (Xu et al., 2007; Wang et al., 2012). The

145 numerical code used in this study has been benchmarked against international

146 standard programs, using SPICE/SISMOWINE. The comparison is provided in the

147 supplementary material.

148 2.3 Source implementation and simulation parameters

149 The seismic moment tensor M_{ij} is the complete representation of an equivalent

150 body-force system for a point source (Gilbert, 1970). It can be decomposed into three

151 fundamental components: isotropy (ISO), double couple (DC), and compensated

152 linear vector dipole (CLVD) (Knopoff and Randall, 1970; Jost and Hermann, 1989).

153 These moment tensor expressions can be written as Eq. (11).

154
$$\boldsymbol{M}^{ISO} = \begin{pmatrix} M_{xx} & 0 & 0 \\ 0 & M_{yy} & 0 \\ 0 & 0 & M_{zz} \end{pmatrix}, \boldsymbol{M}^{DC} = \begin{pmatrix} 0 & M_{xy} & 0 \\ M_{yx} & 0 & 0 \\ 0 & 0 & 0 \end{pmatrix}, \boldsymbol{M}^{CLVD} = \begin{pmatrix} M_{xx} & 0 & 0 \\ 0 & M_{yy} & 0 \\ 0 & 0 & -2M_{zz} \end{pmatrix} \tag{11}$$

155 In our SGFD framework, we follow the method proposed by Graves (1996) to

156 implement the moment tensor source by converting the moment rate tensor into

157 equivalent body forces. The equivalent velocity increment Δv^n added on the grid can

158 be expressed as:

$$\boldsymbol{M}^{ISO} : \Delta v_i^n = \frac{M_{ij} \cdot dt \cdot f^n}{\rho V} \cdot \frac{\partial}{\partial x_j}$$

159
$$\boldsymbol{M}^{DC} : \Delta v_i^n = \frac{M_{jk} \cdot dt \cdot f^n}{\rho V} \cdot (\delta_{ij} \frac{\partial}{\partial x_k} + \delta_{ik} \frac{\partial}{\partial x_j}) \tag{12}$$

$$\boldsymbol{M}^{CLVD} : \Delta v_i^n = \frac{M_{kl} \cdot dt \cdot f^n}{\rho V} \cdot (\delta_{ik} \frac{\partial}{\partial x_l} + \delta_{il} \frac{\partial}{\partial x_k} - \frac{2}{3} \delta_{kl} \frac{\partial}{\partial x_i})$$

160 where $i, j, k, l \in$ {x, y, z}. Δv is the velocity increment, n is the time-step index, dt is

161 the time step, ρ is the density, V is the grid cell volume, and f^n is the value of the

162 source-time function at time n dt.

163   We conduct simulations in a homogeneous, isotropic, 3D full-space model to

164   isolate the effects of nonlinearity from those of complex media. The model parameters

165   are: P-wave velocity v_p=4400 m/s, S-wave velocity v_s=3000 m/s, and density ρ=2600

166   kg/m³. The model space is 14 km $\times$ 14 km $\times$ 14 km, with a uniform grid spacing of Δx

167   = Δy = Δz = 50 m. The source is located at the model center. It uses a Ricker wavelet

168   with a dominant frequency of 4 Hz as the source-time function. Receivers are

169   arranged on a spherical surface with a radius of 5 km centered at the source to sample

170   wavefields at various azimuths. The time step is $\Delta t = 0.0015$s.

171   The shortest wavelength for the 4 Hz dominant frequency is the S-wavelength

172   ($\lambda_S = 750$ m). Based on the 50 m grid spacing, there are 15 grid points per wavelength,

173   which is well above the threshold required for high-order finite-difference schemes

174   (Virieux, 1986). The Courant-Friedrichs-Lewy (CFL) number is approximately 0.23,

175   which is well below the stability limit for 3D finite-difference methods (Moczo et al.,

176   2007), ensuring the stability and accuracy of the numerical computation.

177   3 Comparison of simulation results

178   3.1 Basic characteristics of nonlinear seismic wavefields

179   Fig. 3(a) displays the 6C wavefield snapshots for the ISO source at t=1.5s, while

180   Fig. 3(b) compares the linear and nonlinear waveforms recorded at a specific receiver.

181   Within the framework of linear theory, an ISO source only generates P-waves in

182   homogeneous elastic media. However, a faint signal is still recorded in the P-wave

183   window of the rotational components in the linear simulation (black line). This signal

184 originates from the spatial gradients produced by the wavefront curvature of the

185 near-field P-wave. In the far field, P-wave can be approximated as an irrotational

186 plane wave with no curl in its displacement field. In the near field, however, the

187 spatial gradients of its displacement field can generate weak rotation. This signal is

188 very weak compared to the rotational signals generated by S-waves, and is therefore

189 treated in this study as the baseline background for assessing the nonlinear

190 contributions.

191 The waveform comparison shows that in the S-wave window, the nonlinear

192 simulation exhibits a distinct response with obvious amplitude, whereas the linear

193 simulation is near zero in the ISO results. This vibration is attributed to the P-to-S

194 mode conversion of energy, caused by geometric nonlinearity. Analysis of the

195 waveform characteristics in Fig. 3(b) reveals that the EM caused by nonlinearity is

196 larger in the rotational components than in the translational ones, while the PM is

197 nearly zero. This indicates that the primary effect of geometric nonlinearity is to

198 modulate the energy distribution and envelope shape of the waves, rather than

199 perturbing their fundamental propagation phase. This effect originates from the

200 higher-order nonlinear terms in the strain-displacement relationship. These terms act

201 as new, endogenous body force terms in the wave equation, equivalent to producing

202 minor secondary perturbations in the wave's propagation. These perturbations interact

203 with the primary wavefield, thereby reallocating energy and ultimately altering the

204 wave's amplitude and shape. For instance, as a P-wave from an ISO source

205 propagates, its non-uniform strain field generates spatial gradients. Through the

206   self-interaction of these gradients via the nonlinear terms, an equivalent body force

207   source with a curl component is generated within the medium, which then radiates

208   S-waves.

209

210
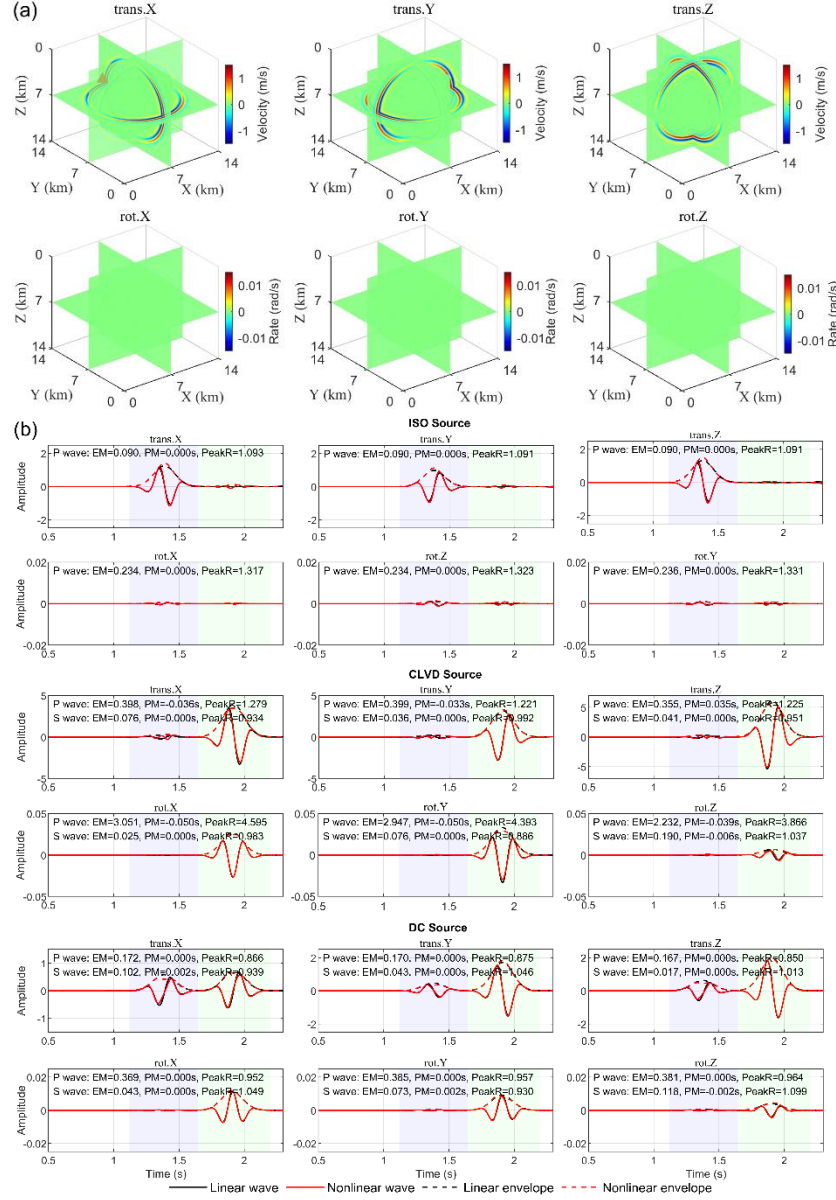
Figure 3. (a) Snapshot of the 6C wavefield from the linear ISO source simulation and

212   the location of the example receiver (indicated by the red triangle on the trans.X

213   component). (b) Comparison of the waveforms and envelope characteristics of the

214   linear and nonlinear simulations at this receiver. The P-wave and S-wave analysis

215   windows are marked. EM: envelope misfit; PM: phase misfit; PeakR: Peak ratio.

216

217   We next calculated the energy of the residual waveforms between the linear and

218   nonlinear simulations. Fig. 4 shows the projection of this metric in the P-wave and

219   S-wave windows onto three principal planes.

220

221
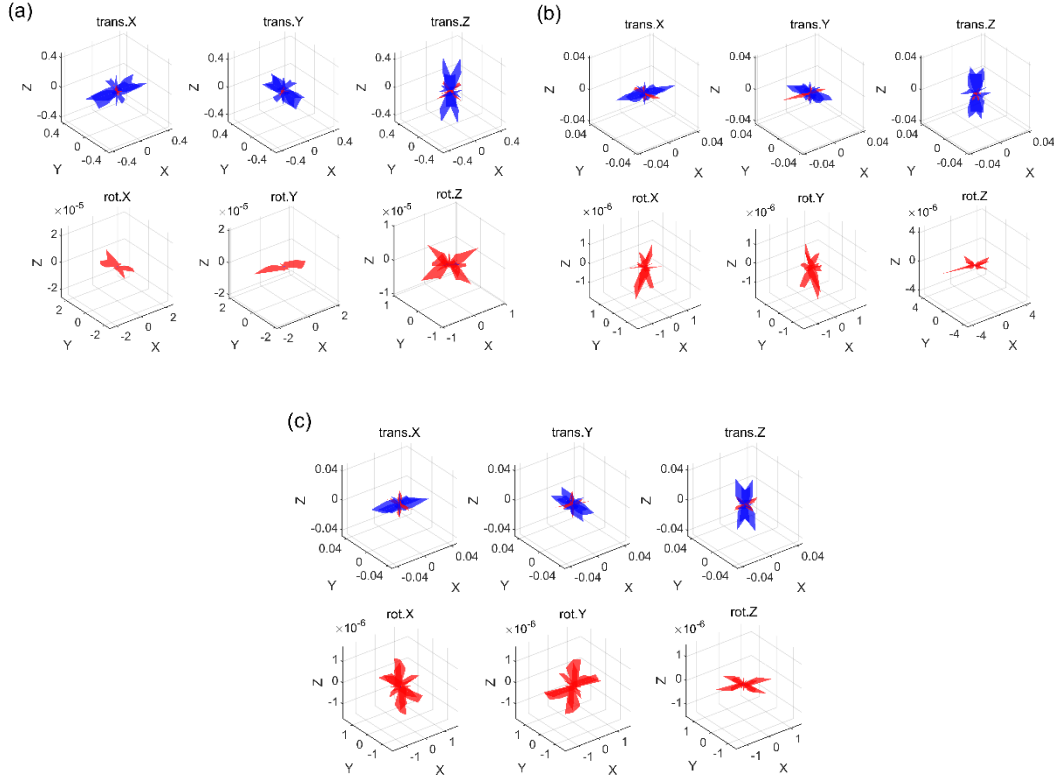
222   **Figure 4.** 3D spatial projection of the intensity of waveform perturbations

223   generated by nonlinearity. (a)-(c) are the results for CLVD, DC, and ISO sources,

224   respectively. Each subplot shows the projection of the nonlinear effect intensity of the

225   P-wave (blue) and the S-wave (red).

226   The results indicate that the radiation of the nonlinear effect follows fundamental

227   wave physics principles. In the translational components, the nonlinear effect of the

228   P-wave is much stronger than that of the S-wave, and its dominant direction is

229   consistent with the corresponding coordinate axes, reflecting the direction of the

230   strongest strain gradient in the linear P-wave field. Consequently, the nonlinear effect

231   is strongest in the direction where the theoretical linear P-wave amplitude projects

232   most strongly onto the corresponding Cartesian component (e.g., the X-axis direction

233   for the trans.X component). In the rotational components, the nonlinear perturbation

234   in the S-wave is dominant. This is because rotational motion is generated by shear

235   strain gradients, and the S-wave, carrying substantial shear energy, is most effective at

236   producing the shear strain gradients required to drive rotation.

237   Building on the time-domain analysis, spectral analysis was conducted on

238   waveforms in the P- and S-wave windows of the median and interquartile range (IQR)

239   of the Power Spectral Density (PSD), as shown in Fig. 5. For the CLVD and DC

240   sources, the median nonlinear spectrum is systematically higher than the median

241   linear spectrum in the mid-to-high frequency band (approx. 5-20 Hz) in both P- and

242   S-waves, and this phenomenon is more pronounced in the rotational components. The

243   translational component spectra are nearly identical in the ISO source simulation. In

244   the S-wave comparison for the ISO source, the linear translational and rotational

245   energies are extremely low, essentially at the level of numerical simulation noise. In

246   contrast, the nonlinear spectrum is several orders of magnitude higher, providing

247   frequency-domain evidence for the nonlinear P-S mode conversion. The IQR of the

248   PSD indicates that the nonlinear effects exhibit strong spatial variability, being

249   enhanced in some azimuths while potentially being weakened in others, thus showing

250   significant azimuthal dependence. The spectral comparison reveals a key feature of

251   the nonlinear effect: energy transfer to higher frequencies. The energy injected by the

252 source, primarily concentrated at lower frequencies, is efficiently pumped by the

253 nonlinear secondary source and re-radiated as higher-frequency energy. This

254 redistribution of high-frequency energy, accompanied by the mode conversion of P-

255 and S-waves, collectively causes the nonlinear spectral lines to be systematically

256 higher than the linear ones in the mid-to-high frequency range.

257
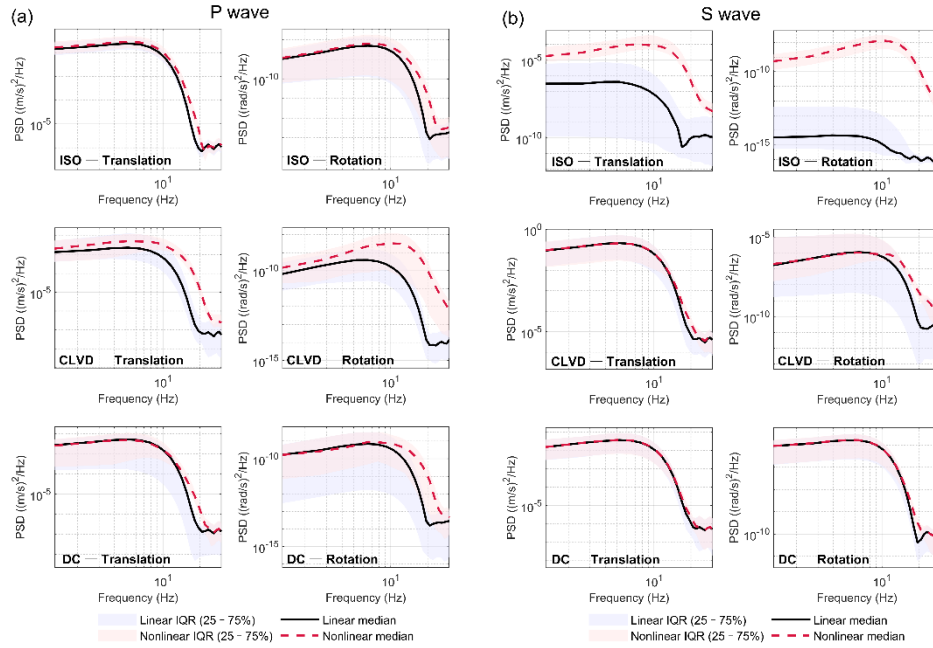
258 **Figure 5.** Comparison of the (a) P-wave and (b) S-wave PSD of translational and

259 rotational components. The black solid line is the median PSD from the linear

260 simulations, the red dashed line is from the nonlinear simulations, and the shaded area

261 represents the 25%-75% IQR.

262 3.1 Source-type dependency of nonlinear effects

263 Fig. 6 presents the log-ratio of nonlinear to linear energy ($\log(E_{nl} / E_{lin})$) for the

264 tangential energy in the P-wave (E^P) and the radial energy in the S-wave (E^S). The

265 energy E is obtained by time-integrating the square of the wavefield amplitude. Fig. 6,

266 through scatter plots and statistics, shows the distribution of the logarithmic energy

267   ratios for the three source types, quantitatively assessing the overall impact of

268   nonlinear effects on the energy of specific wave types.

269   Regarding the tangential energy in the P-wave (Fig. 6(a)), the nonlinear

270   enhancement is most significant for the CLVD source, followed by the DC source,

271   while the effect of the ISO source is minimal. This indicates that the CLVD source is

272   the most effective mechanism for exciting the nonlinear growth of P-wave tangential

273   energy. For the radial energy in the S-wave (Fig. 6(b)), the net effect of nonlinearity

274   for the CLVD and DC sources is not statistically significant, possibly due to the

275   cancellation of azimuthal enhancement and reduction.

276
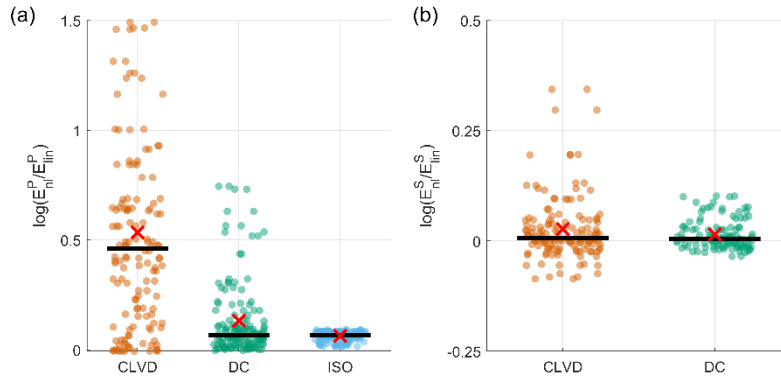
277   **Figure 6.** Distribution of the nonlinear/linear log-ratio for (a) tangential energy

278   in the P-wave and (b) radial energy in the S-wave. The dots represent the values for

279   each independent receiver; the black bar indicates the median of the data; the red

280   cross indicates the arithmetic mean.

281   To further investigate the impact of nonlinearity on the micro-properties of the

282   wavefield, we introduce two quantitative metrics to analyze the waveform attribute

283   changes within the P-wave window. First, we use rectilinearity (rect) to measure the

284   deviation of P-wave particle motion from a straight line. This metric is calculated

285   based on the eigenvalues ($\lambda_1 \geq \lambda_2 \geq \lambda_3$) of the covariance matrix of the

286   three-component particle motion data. While commonly defined as $1 - (\lambda_2 + \lambda_3) / 2\lambda_1$

287   (Jurkevics, 1988), we use a simplified and sensitive form, rect $= (\lambda_1 - \lambda_2) / \lambda_1$. In this

288   formulation, a value approaching 1 indicates purely unidirectional motion, whereas a

289   value close to 0 indicates circular or random motion. The sign of the change, Δrect =

290   rect_{nl} - rect_{lin}, reflects whether the nonlinearity promotes or suppresses the leakage of

291   P-wave energy into the tangential direction. Second, to explore the coupling

292   relationship between different motion modes, we introduce the rotation-translation

293   correlation (corr). This metric is the Spearman's rank correlation coefficient between

294   the time series of the tangential velocity magnitude and the rotation rate magnitude.

295   This non-parametric metric was chosen to robustly quantify the synchrony of the

296   time-varying intensity envelopes. It effectively assesses whether the two intensities

297   trend together (i.e., a monotonic relationship), regardless of the specific functional

298   form linking them (Press et al., 1986).

299   Fig. 7(a) shows the statistical distribution of the differences in these two metrics.

300   For all three sources, Δcorr is generally positive, indicating that geometric

301   nonlinearity may be a common physical mechanism that enhances the coupling

302   between rotation and translation. In contrast, the distribution of Δrect shows a

303   pronounced source dependence: the ISO source causes weak changes, the DC source

304   induces significant negative changes, while the CLVD source primarily causes

305   positive changes. The spatial distribution of Δrect in Fig. 7(b) further reveals its

306   essential connection to the source's strain state. For the ISO source, characterized by

307   pure volumetric strain, the pure volumetric strain excites a very weak shear effect

308   through nonlinearity, leading to a slight decrease in P-wave rectilinearity, but the

309   efficiency of this conversion is extremely low. For the pure-shear DC source, the

310   significant decrease in rectilinearity is concentrated near the P-wave radiation nodes,

311   which are the regions with the strongest linear shear strain gradients. This indicates

312   that in these regions, the efficiency of the nonlinear P-S mode conversion is highest,

313   leading to a noticeable decrease in rectilinearity. For the CLVD source, which

314   combines strong uniaxial compression and axisymmetric shear, the increase in

315   rectilinearity is also concentrated in regions with strong strain gradients. The result

316   reveals that, in a complex stress state with coexisting tension and compression, the

317   nonlinear effect may instead constrain energy to propagate in the radial direction,

318   suppressing leakage into the tangential direction, thereby purifying the P-wave

319   motion.

320

321
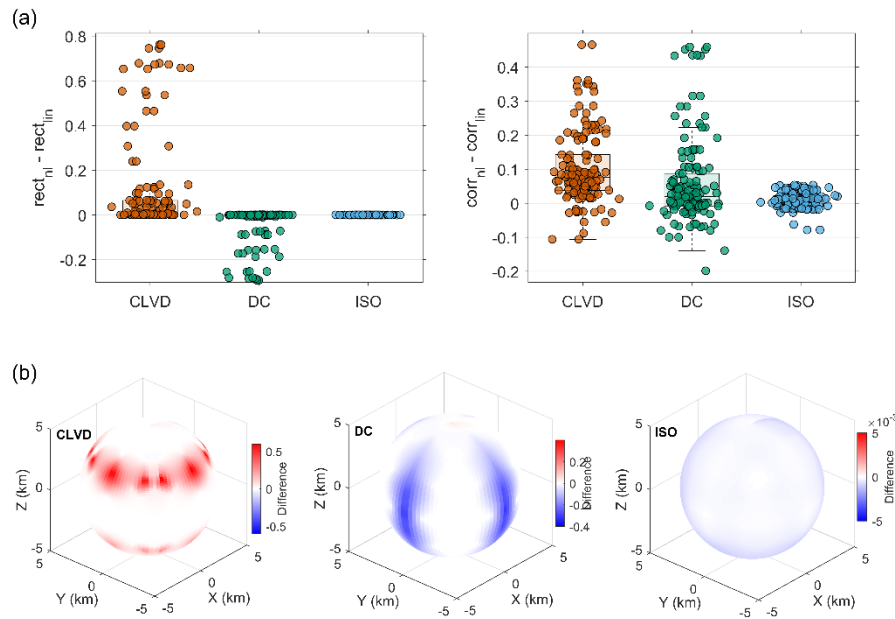
322   **Figure 7.** (a) Statistical distribution of the change in P-wave rectilinearity and

323   rotation-translation correlation changes, and (b) spherical spatial distribution of Δrect

324   in different receivers.

325   In summary, the analysis of the wavefield properties demonstrates that the

326 manifestation of nonlinear effects is fundamentally controlled by the type of strain

327 field initialized by the source and the geometry of its spatial gradients. Different

328 source mechanisms, by initializing different strain fields, thus modulate the mode,

329 intensity, and even the effect of the nonlinear response.

330 4 Simulation of nonlinear effects for referenced earthquake events

331   To extend the understanding established in the idealized full-space model to

332 more realistic scenarios involving complex propagation effects, we further simulate

333 two moderate-to-strong referenced earthquakes that occurred in the coastal region of

334 Taiwan: event E1 (Mw 5.4) and event E2 (Mw 6.1). The epicenters and station

335 locations of these two referenced events are shown in Fig. S3. Unlike the preceding

336 basic source simulations, the models in this section employ a layered velocity

337 structure based on the CRUST1.0 model (Laske et al., 2013) to approximate the real

338 Earth's structure (see Table S4). The source mechanisms for both events (Eq. (13)) are

339 composite, containing both non-double-couple and double-couple components. Other

340 detailed simulation parameters for the two referenced earthquake simulations are

341 provided in Table S5.

$$
\begin{aligned}
E1: &\begin{bmatrix} M_{xx} = -7.569 \times 10^{16}, M_{yy} = -2.373 \times 10^{16}, M_{zz} = 9.942 \times 10^{16} \\ M_{xz} = 7.372 \times 10^{16}, M_{yz} = -1.0965 \times 10^{17}, M_{xy} = 4.156 \times 10^{16} \end{bmatrix} \\
E2: &\begin{bmatrix} M_{xx} = -1.064 \times 10^{18}, M_{yy} = -7.607 \times 10^{17}, M_{zz} = 1.8247 \times 10^{18} \\ M_{xz} = 3.141 \times 10^{17}, M_{yz} = 3.155 \times 10^{17}, M_{xy} = 1.114 \times 10^{18} \end{bmatrix}
\end{aligned}
\tag{13}
$$

342

343   Fig. 8 shows the results for the E1. Compare the waveforms and the

344   time-frequency spectral differences, where the spectra are calculated using a

345   Generalized S-Transform (GST) (Stockwell, 1996), as shown in Fig. 8(b). These

346   differences are defined as the spectra of the nonlinear simulations minus those of the

347   linear simulations. In the translational components, the energy changes induced by

348   nonlinearity are relatively dispersed in different types of waves. However, most are

349   concentrated during the arrival of S-wave (approx. 15-20 s) and the subsequent

350   surface waves, and faint but persistent nonlinear perturbations are also observed

351   during the P-wave and its subsequent multiple reflections/conversions (approx. 5-15

352   s). In the rotational components, the nonlinear response energy is more concentrated

353   than in the translational components. Energy perturbations can be observed on the

354   rot.T component before the direct S-wave arrival, which may correspond to nonlinear

355   effects excited by S-waves converted from P-waves or S-waves reflected/transmitted

356   within the layered medium. For the rot.R and rot.Z components, the nonlinear effects

357   are primarily associated with the arrival of the direct S-wave. Different components

358   showing different extents of nonlinearity may stem from the azimuthal location of this

359   receiver.
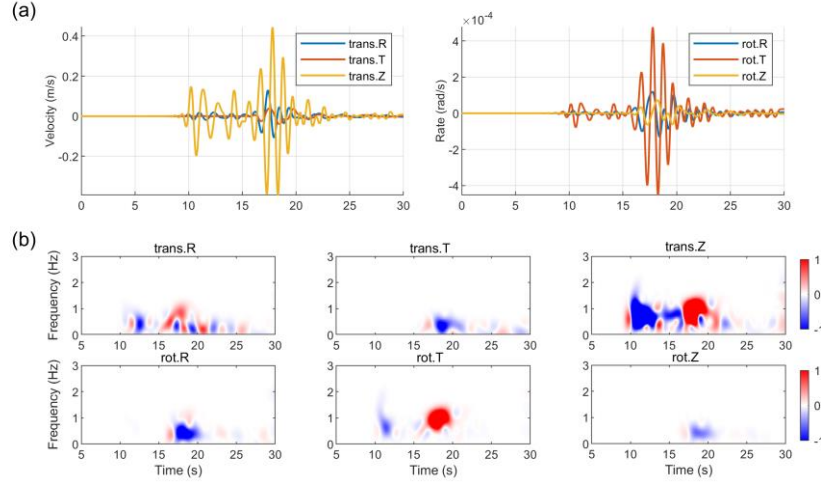
Figure 8. (a) Synthetic linear 6C waveforms (low-pass filtered at 2 Hz) and (b)

normalized time-frequency spectral differences (the nonlinear minus the linear) for

event E1.

Numerical simulations of the E2 (Fig.9) also show nonlinear effects. Combining

the time-domain waveforms (Fig. 9(a)) and the time-frequency spectral energy

difference plots (Fig. 9(b)), it can be seen that significant energy changes occur in all

components during the arrival of the direct S-wave (approx. 90 s) and the strong

surface waves. A long-duration, very-low-frequency (<0.2 Hz) energy enhancement

band appears in the translational components, starting from the surface waves and

continuing. This may correspond to long-period perturbations induced by strong

surface waves through nonlinear mechanisms, potentially involving P-S coupling in

layered media, while the rotational components, as displacement gradients, are not

sensitive to it.
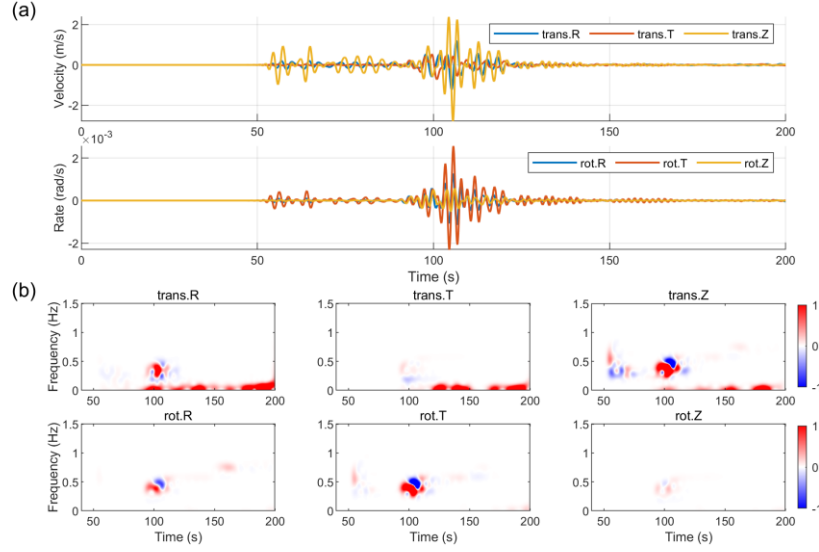
Figure 9. (a) Synthetic linear 6C waveforms (low-pass filtered at 1 Hz) and (b)

normalized time-frequency spectral differences (the nonlinear minus the linear) for

event E2.

By comparing the simulations of the two events, we find that the surface waves

are the primary phases that accumulate and carry nonlinear information. At the same

time, the E2 event, with its different source mechanism and further propagation path,

exhibits a long-period perturbation not seen in the E1 simulation. This suggests that in

more realistic scenarios, the physical mechanisms of nonlinear effects may be more

complex and can be influenced by many factors. The different nonlinear

characteristics displayed by the two event simulations may also be influenced by the

combined effects of their complex, composite source mechanisms and the specific

source-station azimuth.

5 Discussion

This study, through systematic simulations of three basic moment-tensor source

types and referenced earthquake events, has demonstrated several characteristics of

390   geometric nonlinearity in seismic wavefields. First, it demonstrates that the excitation

391   and manifestation of nonlinear effects are controlled by the strain state of the linear

392   wavefield and its spatial gradients. As predicted by nonlinear elastodynamic theory,

393   geometric nonlinearity acts as an equivalent secondary source term in the wave

394   equation, with its strength being proportional to the quadratic terms of the linear strain

395   field. The radiation of nonlinear effects strictly follows the physical nature of

396   longitudinal and transverse waves. For instance, the nonlinear perturbation generated

397   by the strain gradients of a linear P-wave radiates most strongly along the principal

398   direction of the P-wave, whereas the nonlinear rotational effect generated by the

399   shear-strain gradients of an S-wave is most pronounced in regions of maximum

400   S-wave energy. In addition, different source mechanisms (volumetric, pure shear,

401   axisymmetric shear) modulate the mode, strength, and even the effect of the nonlinear

402   response by initializing different geometries of the strain field.

403   Second, rotational motion is a sensitive indicator for detecting near-field

404   nonlinear effects driven by S-waves. This stems from the physical nature of

405   rotation—it is the spatial gradient of the displacement field and is therefore more

406   sensitive to the secondary source terms driven by strain gradients. This suggests that

407   the deployment and analysis of six-component seismic data are of irreplaceable value

408   for identifying and quantifying nonlinear geophysical processes in future

409   observational studies.

410   Finally, the simulations of referenced earthquake events show that surface waves,

411   which are more concentrated in energy and have longer propagation paths, are the

412   primary carriers for accumulating and preserving nonlinear information, thus pointing

413   to a key focus for future observational data analysis. More importantly, in the stronger

414   E2 event, we observed a long-period perturbation not seen in the idealized models.

415   This phenomenon suggests that under realistic strong ground motion conditions, the

416   physical mechanisms of nonlinear effects may be more complex and diverse,

417   potentially involving deeper physical processes such as stress-induced anisotropy.

418   Limitations of this study, such as the use of idealized models, highlight the need for

419   validation with real seismic records. These indicate a direction for future research:

420   how to reliably separate and identify these unique nonlinear signals from collected

421   real seismic records, which is a mixture of complex source effects, 3D heterogeneous

422   propagation effects, and local site responses.

423   6 Conclusions

424   By incorporating geometric nonlinearity based on the Green-Lagrange strain

425   tensor, this study has conducted 6C seismic wavefield simulations for three

426   fundamental moment tensor sources and two referenced moderate-to-strong

427   earthquakes. The research aims to investigate the characteristics of near-field

428   nonlinear effects and their dependence on source mechanisms. The main conclusions

429   are as follows:

430   (i) Universal radiation pattern of the nonlinear secondary source and

431   source-dependent efficiency of exciting the effects. On one hand, the radiation pattern

432   of nonlinearity is universal, strictly adhering to the physics of wave motion: the

433   nonlinear perturbation generated by P-wave strain gradients radiates primarily along

434   the axial direction (a longitudinal characteristic), while the perturbation from S-wave

435   shear-strain gradients radiates mainly in the orthogonal plane directions (a transverse

436   characteristic). This pattern is independent of the initial force source type. On the

437   other hand, the overall efficiency of exciting these nonlinear secondary sources

438   exhibits a strong source-type dependency. Simulation results show that sources with

439   significant shear components, such as CLVD and DC sources, are far more efficient in

440   exciting nonlinear effects than the purely volumetric ISO source.

441   (ii) High sensitivity of rotational motion to S-wave-driven nonlinearity. This is

442   primarily because rotational motion directly responds to shear-strain gradients, and

443   S-waves are the primary carriers of shear energy. Consequently, rotational motion

444   becomes an ideal window for detecting the secondary sources excited by S-waves,

445   with its nonlinear response being more pronounced than that of translational

446   components.

447   (iii) Effects of wave type and strain level. The strength of nonlinear effects is

448   correlated with the strain level (which can be approximately related to the moment

449   magnitude). More importantly, surface waves, which have more concentrated

450   energy and longer propagation paths, are more effective carriers of nonlinear

451   information than body waves. In the strong-motion event simulation, long-period

452   perturbations, possibly induced by nonlinearity, were also observed. This may

453   correspond to long-period perturbations induced by strong surface waves through

454   nonlinear mechanisms, potentially involving P-S coupling in layered media.

455

456 **Author contributions.** WL: conceptualization, methodology, investigation, formal

457 analysis, writing - original draft. YW: conceptualization, writing - original draft and

458 revised draft. CC: investigation, formal analysis. LS: methodology.

459

460 **Data availability.** All data is simulated and available upon reasonable request.

461

462 **Competing interests.** The contact author has declared that neither of the authors has

463 any competing interests.

464

465 **Disclaimer.** Publisher's note: Copernicus Publications remains neutral with regard to

466 jurisdictional claims made in the text, published maps, institutional affiliations, or any

467 other geographical representation in this paper.

468

469 **Financial support.** This research is financially supported by the National Natural

470 Science Foundation of China (No. 42150201、No. 62127815、No. U1839208).

471

472 **Acknowledgements.** We are grateful to the handling editor and anonymous reviewers

473 for their time and feedback, which have greatly improved the quality of this

474 manuscript.

475

476 References

477 Aki, K., and P. G. Richards. Quantitative seismology, 2nd ed, California: University

478   Science Books, https://doi.org/10.1029/2003EO210008, 2002.

479   Bernauer, M., Fichtner, A., and Igel, H.: Reducing nonuniqueness in finite source

480   inversion using rotational ground motions, J. Geophys. Res.-Solid Earth, 119(6),

481   4860-4875, https://doi.org/10.1002/2014JB011042, 2014.

482   Bonilla, L. F., Archuleta, R. J., and Lavallée, D.: Hysteretic and dilatant behavior of

483   cohesionless soils and their effects on nonlinear site response: Field data

484   observations and modeling. Bull. Seismol. Soc. Am., 95(6), 2373-2395.

485   https://doi.org/10.1785/0120040138, 2005.

486   Bonilla, L. F., Tsuda, K., Pulido, N., Régnier, J., and Laurendeau, A.: Nonlinear site

487   response evidence of K-NET and KiK-net records from the 2011 off the Pacific

488   coast of Tohoku Earthquake. Earth, Planets and Space, 63(7), 785-789.

489   https://doi.org/10.5047/eps.2011.06.012, 2011.

490   Donner, S., Bernauer, M., and Igel, H.: Inversion for seismic moment tensors

491   combining translational and rotational ground motions, Geophys. J. Int., 207(1),

492   562-570, https://doi.org/10.1093/gji/ggw298, 2016.

493   Feng, X., Fehler, M., Brown, S., Szabo, T. L., and Burns, D.: Short-period nonlinear

494   viscoelastic memory of rocks revealed by copropagating longitudinal acoustic

495   waves, J. Geophys. Res.-Solid Earth, 123(5), 3993–4006,

496   https://doi.org/10.1029/2017JB015012, 2018.

497   Frankel, A. D., Carver, D. L., and Williams, R. A.: Nonlinear and linear site response

498   and basin effects in Seattle for the M 6.8 Nisqually, Washington, earthquake.

499   Bull. Seismol. Soc. Am., 92(6), 2090-2109. https://doi.org/10.1785/0120000738,

500   2002.

501   Graizer, V. M.: Strong motion recordings and residual displacements: what are we

502   actually recording in strong motion seismology? Seismol. Res. Lett., 8(4),

503   635-639, https://doi.org/10.1785/gssrl.81.4.635, 2010.

504   Graizer, V. M.: Inertial seismometry methods, Earth Physics, 27(1), 51-61, 1991.

505   Graves, R. W.: Simulating seismic wave propagation in 3D elastic media using

506   staggered-grid finite differences, Bull. Seismol. Soc. Am., 86(4), 1091-1106,

507   1996.

508   Gilbert, F.: Excitation of the normal modes of the Earth by earthquake sources,

509   Geophys.   J.   R.   astr.   Soc,   22(2),   223-226,

510   https://doi.org/10.1111/j.1365-246X.1971.tb03593.x, 1970.

511   Hua, S. B., and Zhang, Y.: Numerical experiments of moment tensor inversion with

512   rotational   ground   motions,   Chinese   J.   Geophys.,   65(1),   197-213,

513   https://doi.org/10.6038/cjg2022P0668, 2022 (in Chinese).

514   Huras, L., Zembaty, Z., Bonkowski, P. A., and Bobraet, P.: Quantifying local stiffness

515   loss in beams using rotation rate sensors, Mech. Syst. Signal Proc., 151, 107396,

516   https://doi.org/10.1016/j.ymssp.2020.107396, 2021.

517   Ichinose, G. A., Ford, S. R., and Mellors, R. J.: Regional moment tensor inversion

518   using   rotational   observations,   J.   Geophys.   Res.-Solid   Earth,   126(2),

519   e2020JB020827, https://doi.org/10.1029/2020JB020827, 2021.

520   Jost, M. L., and Hermann, R. B.: A students guide to and review of moment tensors,

521   Seism. Res. Lett., 60, 37-57, https://doi.org/10.1785/gssrl.60.2.37, 1989.

522 Jurkevics, A.: Polarization analysis of three-component array data, Bull. Seismol. Soc.

523   Am., 78 (5), 1725–1743, https://doi.org/10.1785/BSSA0780051725,1988.

524 Knopoff, L., and Randall M. J.: The compensated linear-vector dipole: A possible

525   mechanism for deep earthquakes, J. Geophys. Res., 75(26), 4957–4963,

526   https://doi.org/10.1029/JB075i026p04957, 1970.

527 Kozak, J. T.: Tutorial on earthquake rotational effects: historical examples, Bull.

528   Seismol. Soc. Am., 99(2B), 998-1010, https://doi.org/10.1785/0120080308,

529   2009.

530 Laske, G., Masters, G., Ma, Z. T., and Pasyanos, M.: Update on CRUST1. 0-A

531   1-degree global model of Earth's crust, EGU General Assembly 2013, 15,

532   EGU2013-2658, 2013.

533 Lee, W. H. K., Igel, H., Todorovska, M. I., and Trifunac, M. D.: Recent advances in

534   rotational seismology, Seismol. Res. Lett., 80(3), 479–490,

535   https://doi.org/10.1785/gssrl.80.3.479, 2009.

536 Li, H. N.: Study on rotational components of ground motion, Journal of Shenyang

537   Architectural and Civil Engineering Institute, 7(1), 88-93, 1991 (in Chinese).

538 Li, H. N., and Sun, L. Y.: Rotational components of earthquake ground motions

539   derived from surface waves, Earthq. Eng. Eng. Vib., 21(1), 15-23,

540   https://link.oversea.cnki.net/doi/10.13197/j.eeev.2001.01.003, 2001 (in Chinese).

541 Li, P. X., Lin, W. J., Zhang, X. M., and Wang, X. M.: Comparisons for regular

542   splitting and non-splitting perfectly matched layer absorbing boundary

543   conditions. Acta Acustica, 40(01), 44-53,

544   https://link.oversea.cnki.net/doi/10.15949/j.cnki.0371-0025.2015.01.006, 2015.

545   Press, W., Flannery, B., Teukolsky, S., and Vetterling, W.: Numerical recipes: The art

546   of scientific computing, Cambridge University Press, 1986.

547   Régnier, J., Bonilla, L. F., Bard, P. Y., et al.: PRENOLIN: International benchmark

548   on 1D nonlinear site-response analysis—Validation phase exercise. Bull.

549   Seismol. Soc. Am., 108(2), 876-900. https://doi.org/10.1785/0120170210, 2018.

550   Renaud, G., Le Bas, P. Y., and Johnson, P. A.: Revealing highly complex elastic

551   nonlinear (anelastic) behavior of Earth materials applying a new probe: Dynamic

552   acoustoelastic testing, J. Geophys. Res.-Solid Earth, 117, B06202,

553   https://doi.org/10.1029/2011JB009127, 2012.

554   Renaud, G., Rivière, J., Le Bas, P. Y., and Johnson, P. A.: Hysteretic nonlinear

555   elasticity of Berea sandstone at low-vibrational strain revealed by dynamic

556   acoustoelastic testing, Geophys. Res. Lett., 40(4), 715-719,

557   https://doi.org/10.1002/grl.50150, 2013.

558   Stockwell, R. G., Mansinha, L., and Lowe, R. P.: Localization of the complex

559   spectrum: the S transform, IEEE Transactions on Signal Processing, 44(4),

560   998-1001, https://doi.org/10.1109/78.492555. 1996.

561   Sun, L., Yu, Y., Lin, J. Q., and Liu, J. L.: Study on seismic rotation effect of simply

562   supported skew girder bridge, Earthquake Engineering and Engineering

563   Dynamics, 37(4), 121-128, https://doi.org/10.13197/j.eeev.2017.04.121.sunl.014,

564   2017 (in Chinese).

565   Sun, L. X., Zhang, Z., and Wang, Y.: Six-component elastic-wave simulation and

566   analysis, EGU General Assembly 2018, Geophysical Research Abstracts, 20,

567   EGU2018-14930-1, 2018.

568   TenCate, J. A., Malcolm, A. E., Feng, X., and Fehler, M. C.: The effect of crack

569   orientation on the nonlinear interaction of a P wave with an S wave, Geophys.

570   Res. Lett., 43(12), 6146-6152, https://doi.org/10.1002/2016GL069219, 2016.

571   Tromp, J., and Trampert, J.: Effects of induced stress on seismic forward modelling

572   and   inversion.   Geophys.   J.   Int.,   213(2),   851-867.

573   https://doi.org/10.1093/gji/ggy020, 2018.

574   Virieux, J.: P-SV wave propagation in heterogeneous media; velocity-stress

575   finite-difference   method,   Geophysics,   51(4),   889-901,

576   https://doi.org/10.1190/1.1442147, 1986.

577   Xu, Y. X., Xia, J. H., and Miller, R. D.: Numerical investigation of implementation of

578   airearth boundary by acoustic-elastic boundary approach, Geophysics, 72 (5),

579   SM147–SM153, https://doi.org/10.1190/1.2753831, 2007.

580   Yan, Y. Y.: Seismic response analysis of high-rise building under different types of

581   multi-dimensional earthquake ground motions (Ph.D. dissertation), Jiangsu

582   University, 2017(in Chinese).

583   Zhou, C., Zeng, X. Z., Wang, Q. L., Liu, W. Y., and Wang, C. Z.: Rotational motions

584   of the Ms7.0 Jiuzhaigou earthquake with ground tilt data, Science China Earth

585   Science, 62(5), 832-842, https://doi.org/10.1007/s11430-018-9320-3, 2019.

586